



A novel Cu-based covalent organic framework with Cu-N₂O₂ single sites for efficient CO₂ electroreduction to methane

Wenli Su, Shuxin Zhong, Yu Fan^{*}

State Key Laboratory of Heavy Oil Processing, China University of Petroleum, Beijing 102249, PR China

ARTICLE INFO

Keywords:

CO₂ electroreduction

Methane

Covalent organic framework

Cu-N₂O₂ single sites

Density functional theory

ABSTRACT

Single-site catalysts (SSCs) are useful for CO₂ electroreduction (CO₂ER) to methane (CH₄), but their selectivities for CH₄ are still unsatisfactory due to the lack of efficient active sites. Herein, a novel Cu-based covalent organic framework (CuN₂O₂-COF) with Cu-N₂O₂ single sites was synthesized by the Schiff base reaction and used in CO₂ER to improve CH₄ generation for the first time. Compared with typical SSCs containing Cu-N₄ or Cu-O₄ sites, CuN₂O₂-COF exhibited superior CH₄ production efficiency in CO₂ER: the Faradaic efficiency of CH₄ was as high as 85.4%, and the CH₄ partial current density reached 313 mA·cm⁻² at -1.3 V, which exceeded those of most electrocatalysts reported thus far. Theoretical calculations indicated that compared with the Cu-N₄ or Cu-O₄ sites in typical SSCs, the new Cu-N₂O₂ configuration in CuN₂O₂-COF increased the d-band center of the Cu sites and enhanced the adsorption of key intermediates (*COOH and *CHO) required for CO₂ER to CH₄.

1. Introduction

Electroreduction of excess CO₂ in the atmosphere to high-value-added products could alleviate global climate warming and store renewable energy [1,2]. As one of the main hydrocarbon products from CO₂ electroreduction (CO₂ER), methane (CH₄) has attracted significant attention due to its compatibility with existing infrastructure and the prospect of replacing fossil fuels [3,4]. However, the extremely stable molecular structure of CO₂, the many CO₂ byproducts formed during the CO₂ER and the competition with the hydrogen evolution reaction (HER) in aqueous solutions are great obstacles to the conversion of CO₂ into CH₄ [5]. It is essential to develop advanced CO₂ER electrocatalysts with high activities and selectivities as well as good stabilities to solve the abovementioned issues.

To date, except for a few Sn-based [6] and Zn-based [7] materials, the catalysts that facilitate reduction of CO₂ to CH₄ are mainly metallic Cu or Cu-based materials, including nanoscale Cu clusters [8,9] or Cu oxides [10], sulfides [11], alloys [12,13], and composites [14–16]. However, it is usually difficult to achieve high CH₄ selectivity with these traditional Cu-based electrocatalysts due to the inevitable dimerization of intermediates such as *CO or *COH, resulting in the formation of multicarbon products such as ethylene (C₂H₄) [17,18]. The construction of single-site electrocatalysts to spatially separate the catalytically active centers is an effective way to suppress C-C coupling [19–21]. Among

these catalysts, Cu-based single-atom catalysts (SACs) obtained by carbonizing Cu-containing precursors are typical single-site electrocatalysts [22–24]. Guan et al. prepared a series of Cu SACs with Cu-N_x sites via high-temperature pyrolysis and reported that the catalysts exhibited CH₄ generation during CO₂ER when the Cu-N_x sites were far from each other [25]. However, the Cu loadings in current SACs are usually low (<5.0 wt%), which results in inferior activity in the CO₂ER [26,27]. Increased Cu loadings led to close proximity and even agglomeration of Cu single atoms, which caused dimerization of intermediates such as *CO, and the reaction path was transferred from the formation of CH₄ to the formation of multicarbon products [25]. Therefore, it is challenging to simultaneously improve the activities and selectivities of Cu-based SACs for CO₂ER to CH₄.

In recent years, Cu-based organic framework materials, including metal organic frameworks (MOFs) and covalent organic frameworks (COFs), which are also single-site electrocatalysts, have shown promise for use in the CO₂ER to CH₄ [28–30]. Similar to SACs, Cu-based MOFs and COFs also have atomically dispersed active sites, which suppress C-C coupling in the CO₂ER [31,32]. More importantly, the structures of the Cu-based MOFs and COFs (especially the density and coordination environment of Cu sites) can be tailored with their functionalized ligands [29,33,34], which is important for optimizing the performance of catalysts and establishing clear structure-activity relationships. Several reports have shown that COF catalysts based on copper phthalocyanine

^{*} Corresponding author.

E-mail address: fanyu@cup.edu.cn (Y. Fan).

<https://doi.org/10.1016/j.apcatb.2024.124145>

Received 27 February 2024; Received in revised form 17 April 2024; Accepted 30 April 2024

Available online 3 May 2024

0926-3373/© 2024 Elsevier B.V. All rights reserved.

or copper porphyrin exhibited considerable selectivity for CH₄ in the CO₂ER because the spatially separated Cu–N₄ sites in the catalysts facilitated the protonation of *CO to *CHO rather than dimerization coupling of *CO [35–37]. In addition to the monodisperse active sites, the coordination environments of the metal centers in Cu-based MOF/COF materials also have a significant effect on the product distribution of CO₂ER [38]. With theoretical calculations, Lan et al. noted that the energy barrier for CO₂ER to CH₄ at Cu–O₄ sites was lower than that at N-coordinated Cu sites [39]. Therefore, the Cu-based MOF catalyst (Cu-DBC) prepared with Cu–O₄ sites as the active centers had a greater selectivity for CH₄ than phthalocyanine- or porphyrin-based catalysts containing Cu–N₄ sites [39]. The current Cu-based MOF/COF catalysts exhibiting good performance in the CO₂ER are basically composed of Cu–O₄ or Cu–N₄ sites, but the Faradaic efficiencies (FEs) for CH₄ with most reported electrocatalysts are still unsatisfactory. Regulation of the coordinated configuration of Cu sites in Cu-based MOFs/COFs is an effective way to promote the formation of CH₄ in the CO₂ER, since it could optimize the electronic structures of the Cu sites and thereby enhance the adsorption of key intermediates. Given this, a novel Cu-based COF material with N- and O-coordinated Cu sites was synthesized in this work, and it was applied in the CO₂ER to improve the efficiency of CH₄ generation for the first time.

The Cu-based COF material (CuN₂O₂-COF) with Cu–N₂O₂ single sites was prepared by a facile Schiff base reaction, and its electrocatalytic performance in the CO₂ER was tested. Then, typical Cu-based MOFs/COFs containing Cu–N₄ or Cu–O₄ sites were used as reference catalysts to investigate the influences of the coordination configurations of Cu sites in the Cu-based MOF/COF materials on their CO₂ER performance. Finally, the reaction pathway of CO₂ER to CH₄ on the novel CuN₂O₂-COF and the reasons for its high CH₄ selectivity were analyzed by in situ infrared spectroscopy and theoretical calculations.

2. Experimental section

2.1. Chemicals and materials

Anhydrous cupric acetate [Cu(CH₃COO)₂, 98%], acetic acid (CH₃COOH, 99.5%), 1,2,4,5-benzenetetraamine tetrahydrochloride (BAT, 97%), 2,5-dihydroxy-1,4-benzenedicarboxaldehyde (HBC, 97%), cupric nitrate [Cu(NO₃)₂, 97%], copper(II) phthalocyanine (CuPc, 99%), tetrahydroxyquinone (THQ, 98%), N,N-dimethylformamide (DMF, 99.9%), 1-methyl-2-pyrrolidinone (NMP, 98%), methanol (CH₃OH, 99.5%), potassium bicarbonate (KHCO₃, 99.99%), isopropanol (99.9%), and potassium hydroxide (KOH, 99.99%) were purchased from Shanghai Aladdin Biochemical Co., Ltd. Nitrogen (N₂, 99.999%) and carbon dioxide (CO₂, 99.999%) were purchased from Beijing Haipu Gas Co., Ltd. Nafion solution (DuPont, D-520 dispersion, 5% w/w in water, and 1-propanol) and a proton exchange membrane (Nafion® 117, DuPont) were purchased from Alfa Aesar. The gas diffusion layer (YSL-30 T) and anion-exchange membrane (Fumatech FAA-3-50) were purchased from Suzhou Sinero Technology Co., Ltd. All chemical reagents and gases were used directly without further purification.

2.2. Preparation of catalysts

2.2.1. Syntheses of CuN₂O₂-COF and N₂O₂-COF

NMP (5 mL) was added to a glass vial (volume of 10 mL), and then HBC (166 mg, 1 mmol), BAT (142 mg, 0.5 mmol) and Cu(CH₃COO)₂ (363 mg, 2 mmol) were added and stirred for 4 h to obtain a uniform dispersion. The vials were transferred to a 100 mL Teflon-lined stainless steel autoclave, sealed and heated at 120 °C for 72 h. After cooling to room temperature, the black precipitate was collected by centrifugation, washed three times with DMF and CH₃OH, and finally dried in a vacuum oven at 80 °C for 12 h. The obtained material was labeled CuN₂O₂-COF.

In addition, the Cu-free COF material (N₂O₂-COF) was synthesized via the same procedure used for CuN₂O₂-COF, except that Cu(CH₃COO)₂

was replaced with CH₃COOH (Fig. S1).

2.2.2. Synthesis of Cu-THQ

THQ (225 mg) was dissolved in H₂O (75 mL) under N₂ protection. Cu(NO₃)₂ (320.3 mg) and ethylenediamine (172.5 μL) were mixed in degassed H₂O (75 mL) and transferred to the THQ solution under vigorous stirring. The mixture was stirred at 25 °C for 12 h under N₂ protection. The dark navy precipitate was centrifuged, washed three times with H₂O and CH₃OH, and dried in a vacuum oven at 80 °C for 12 h. The obtained material was labeled Cu-THQ.

2.3. Characterization

Structural characterization of the catalysts involved X-ray diffraction (XRD), Fourier transform infrared (FT-IR) spectroscopy, X-ray photoelectron spectroscopy (XPS), inductively coupled plasma optical emission spectroscopy (ICP–OES), solid-state ¹³C cross-polarization magic-angle-spinning nuclear magnetic resonance (¹³C CP-MAS NMR) spectroscopy, scanning electron microscopy (SEM), transmission electron microscopy (TEM), high-resolution transmission electron microscopy (HRTEM), aberration-corrected high-angle annular dark-field scanning transmission electron microscopy (HAADF-STEM) with energy dispersive X-ray spectroscopy (EDS), and Cu K-edge synchrotron X-ray absorption spectroscopy (XAS). For the XAS characterization, the X-ray absorption near-edge structure (XANES) and extended X-ray absorption fine structure (EXAFS) spectra were processed with the Athena program and then fitted for analysis by the Artemis program [40]. Moreover, the intermediates during CO₂ER were detected by in situ electrochemical attenuated total reflection Fourier transform infrared (ATR-FTIR) spectroscopy. The detailed methods of the above characterizations are described in the [Supplementary Information](#).

2.4. Electrochemical measurements

The methods for evaluating the CO₂ER performances of the catalysts are described in the [Supplementary Information](#).

3. Results and discussion

3.1. Characterization of CuN₂O₂-COF and N₂O₂-COF

A new CuN₂O₂-COF material with Cu–N₂O₂ active sites was synthesized in NMP by a solvothermal method with BAT, HBC, and Cu(CH₃COO)₂ as the raw materials (Fig. 1a). The FT-IR spectra showed that a signal at 1623 cm^{−1} for the C=N bond appeared in the CuN₂O₂-COF and N₂O₂-COF spectra, while the signal at 1673 cm^{−1} for the C=O bonds of the aldehyde groups disappeared (Fig. 1b), indicating that the amino group of BAT and the aldehyde group of HBC were successfully condensed into imines via the Schiff base reaction [41,42]. In the solid-state ¹³C CP-MAS NMR spectrum of CuN₂O₂-COF, the peaks in the range of 114–124 ppm were attributed to aromatic carbon atoms [43], and the peak at 155 ppm was attributed to imine carbon atoms (Fig. 1c) [44], which was consistent with the peak observed for N₂O₂-COF (Fig. S2). The above FT-IR and ¹³C CP-MAS NMR results confirmed the formation of an imine network in the CuN₂O₂-COF and N₂O₂-COF.

There were no diffraction peaks related to metallic Cu or oxidized Cu species in the XRD pattern of CuN₂O₂-COF (Fig. S3), but the ICP–OES results showed that the Cu content in CuN₂O₂-COF reached 9.7 wt% (Table S1), which demonstrated the high loading of Cu sites in CuN₂O₂-COF. The SEM and TEM images showed that CuN₂O₂-COF was composed of wrinkled sheets (Fig. 2a and b), which was consistent with the structure of N₂O₂-COF (Fig. S4). Notably, there were no metallic clusters in the HRTEM image of CuN₂O₂-COF (Fig. 2c), whereas the aberration-corrected HAADF-STEM image revealed a large number of isolated bright spots for CuN₂O₂-COF (Fig. 2d), indicating that the Cu atoms were uniformly dispersed in the CuN₂O₂-COF catalyst as single

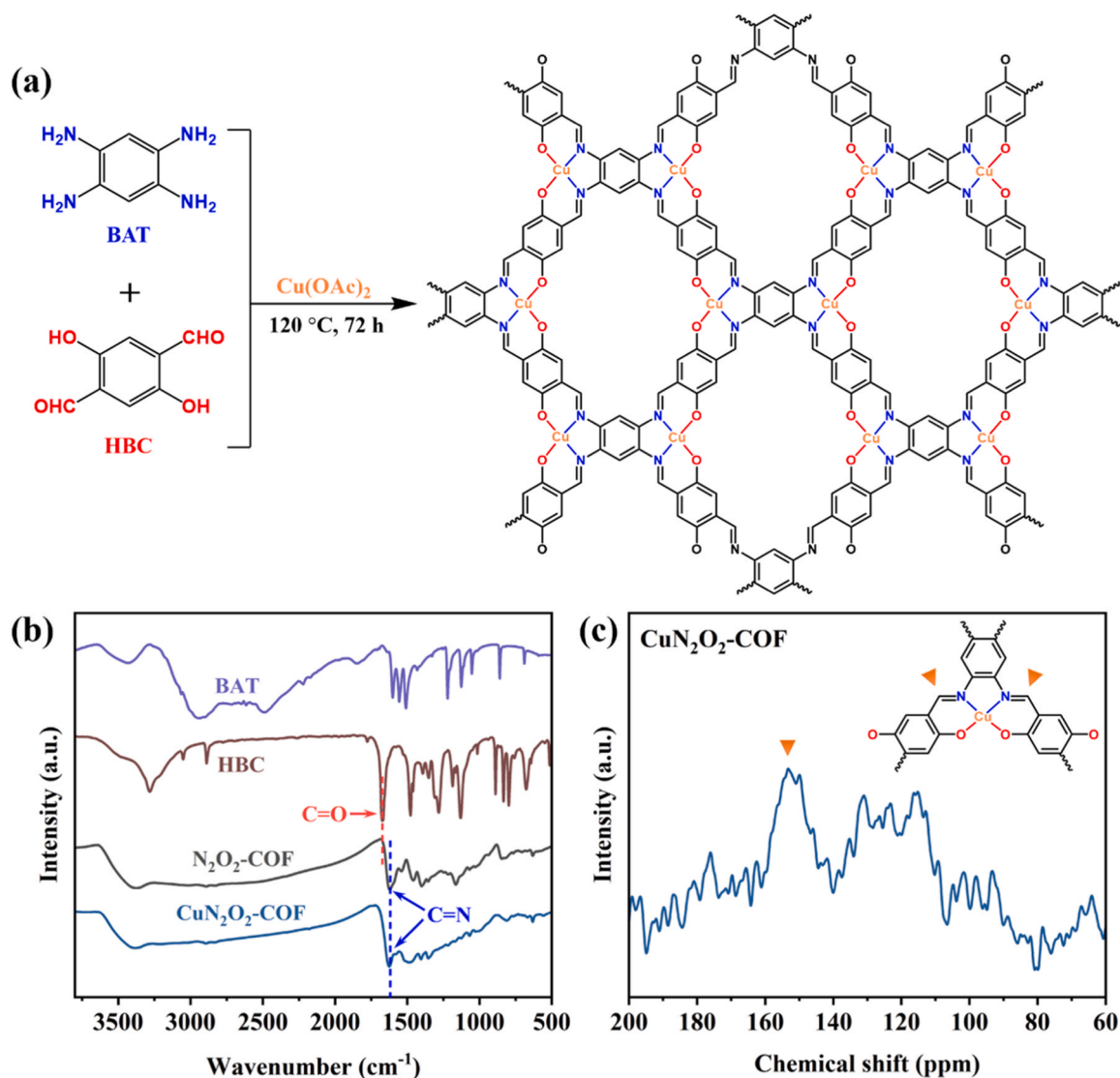


Fig. 1. Schematic diagram of the CuN₂O₂-COF synthesis (a); FT-IR spectra of BAT, HBC, N₂O₂-COF and CuN₂O₂-COF (b); solid-state ¹³C CP-MAS NMR spectrum of CuN₂O₂-COF (c).

sites. The corresponding EDS element maps also confirmed the homogeneous distributions of Cu, N, O and C in the CuN₂O₂-COF (Fig. 2e).

XPS showed that N₂O₂-COF contained C, N and O, while CuN₂O₂-COF contained C, N, O and Cu (Fig. S5). The Cu content in CuN₂O₂-COF was approximately 10.8 wt% (Table S1), which was close to the ICP-OES result. The Cu 2p spectrum in Fig. 3a revealed the chemical states of the Cu species on the CuN₂O₂-COF. Two dominant peaks at 934.6 and 954.4 eV were assigned to Cu(II), and the satellite peaks at 939.3, 943.6 and 962.9 eV also confirmed the presence of Cu(II), whereas the other two smaller peaks at 932.3 and 952.4 eV were attributed to Cu(I) or Cu(0) [45]. The Cu LMM Auger spectrum in Fig. 3b proved that the Cu species on CuN₂O₂-COF were mainly Cu(II) and a small amount of Cu(I) without Cu(0) species. The Cu(I) species in CuN₂O₂-COF may have originated from the reduction of unsaturated Cu (II) at the framework defects of the COF [46].

The oxidation states and local coordination environments of the Cu species in CuN₂O₂-COF were investigated by synchrotron XAS of the Cu K-edge, and the results are shown in Fig. 4. The Cu K-edge XANES spectra showed that the white line peak for CuN₂O₂-COF was located between those for the standard reference Cu₂O and CuO (Fig. 4a), and the peak for CuN₂O₂-COF in the first derivative of the XANES spectrum was also located in the region between Cu(I) and Cu(II) (Fig. 4b),

indicating that the average valence of the Cu atoms in CuN₂O₂-COF was between +1 and +2. The Fourier transform Cu K-edge EXAFS spectra in Fig. 4c revealed the fine coordination structures of the Cu atoms in CuN₂O₂-COF. The peak at 1.50 Å was attributed to the Cu-N/O bond in CuN₂O₂-COF, and there was no peak at 2.23 Å corresponding to a Cu-Cu bond [25,47], indicating that the Cu atoms in CuN₂O₂-COF were spatially separated and coordinated with N or O atoms. Finally, the EXAFS spectrum of CuN₂O₂-COF was analyzed by fitting, and the fitting parameters are shown in Table S2. The fitting results in Fig. 4d and S6 proved that the Cu atoms in CuN₂O₂-COF were coordinated with two N atoms and two O atoms, and the bond lengths of Cu-O and Cu-N were 1.87 and 2.01 Å, respectively. The above XAS results confirmed that the Cu atoms in CuN₂O₂-COF were coordinated with N and O atoms. Therefore, this CuN₂O₂-COF catalyst with Cu-N₂O₂ single sites is expected to exhibit superior electrocatalytic performance in the CO₂ER.

Furthermore, the synthesis method for CuN₂O₂-COF can be extended to other transition metals (such as Co and Ni), because the vacant orbitals in these transition metal ions are able to interact with the lone pair electrons in the N₂O₂ configuration.

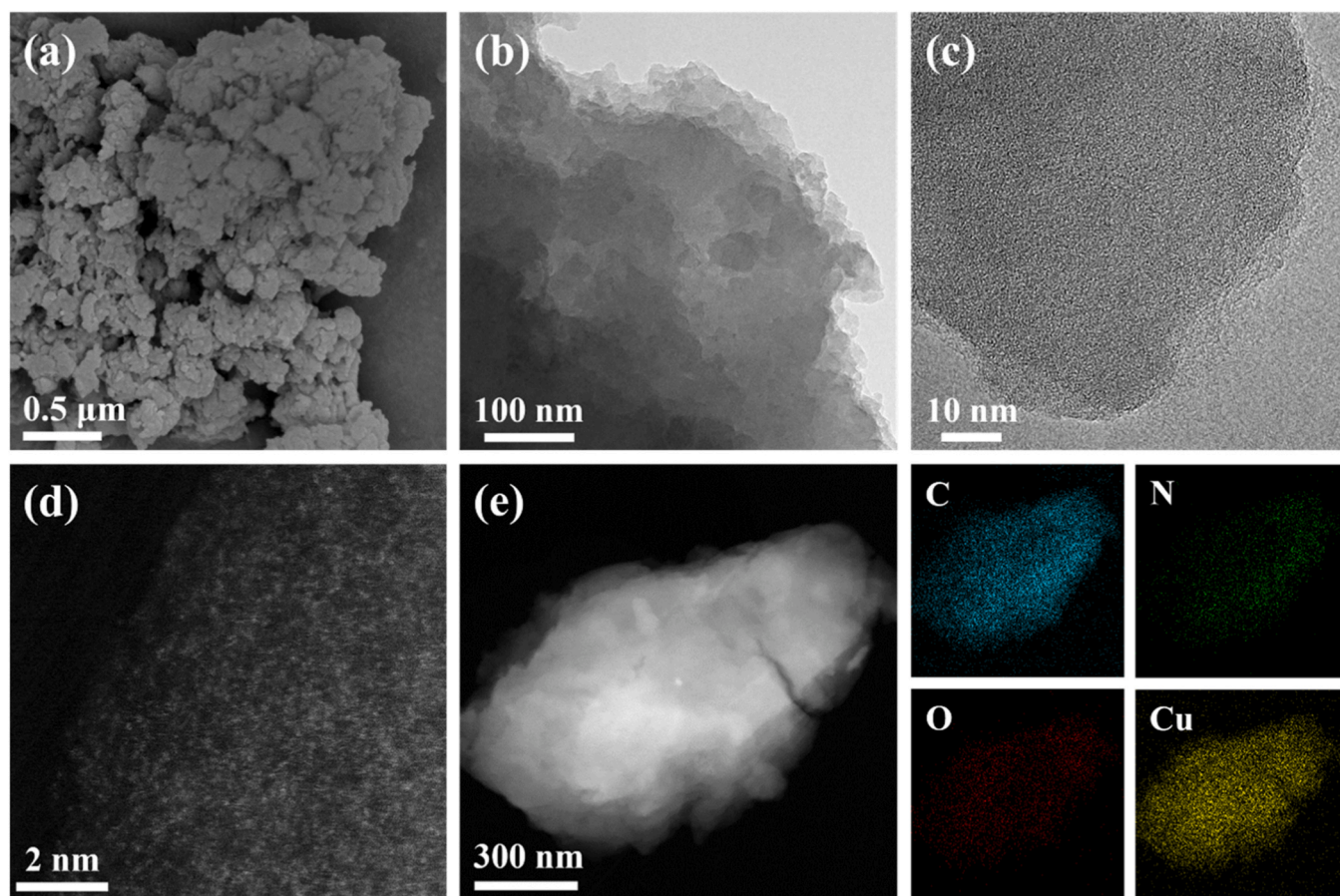


Fig. 2. SEM image (a), TEM image (b), HRTEM image (c), aberration-corrected HAADF-STEM image (d), and corresponding EDS elemental maps (e) of CuN₂O₂-COF.

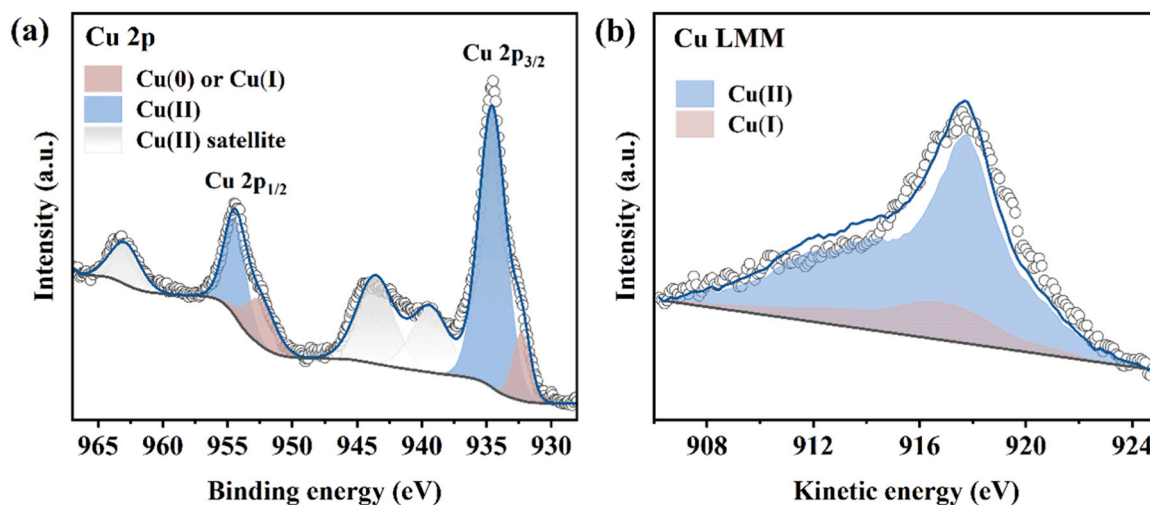


Fig. 3. Cu 2p (a) and Cu LMM Auger (b) XPS spectra of CuN₂O₂-COF.

3.2. CO₂ER performance of CuN₂O₂-COF and N₂O₂-COF

To evaluate the electrocatalytic performance of the two catalysts, linear scanning voltammetry (LSV) and potentiostatic electrolysis were first performed in a typical H-type cell (Fig. S7) configured with a standard three-electrode system and a proton-exchange membrane with a 0.5 M KHCO₃ aqueous solution as the electrolyte. All potentials herein were versus the reversible hydrogen electrode (vs. RHE) unless otherwise noted. The LSV polarization curves in Fig. 5a show that N₂O₂-COF

and CuN₂O₂-COF had higher current densities in the CO₂-saturated electrolyte than in the N₂-saturated electrolyte, which confirmed the occurrence of CO₂ER. More importantly, CuN₂O₂-COF exhibited a more positive onset potential and much higher current density than N₂O₂-COF in the CO₂-saturated electrolyte, indicating that the Cu single sites in CuN₂O₂-COF provided the catalytic activity for CO₂ER.

The product selectivities of the two catalysts in CO₂ER were determined by potentiostatic electrolysis in the potential range −1.0 to −1.5 V. As shown in Fig. 5b, the products of the N₂O₂-COF catalyst were

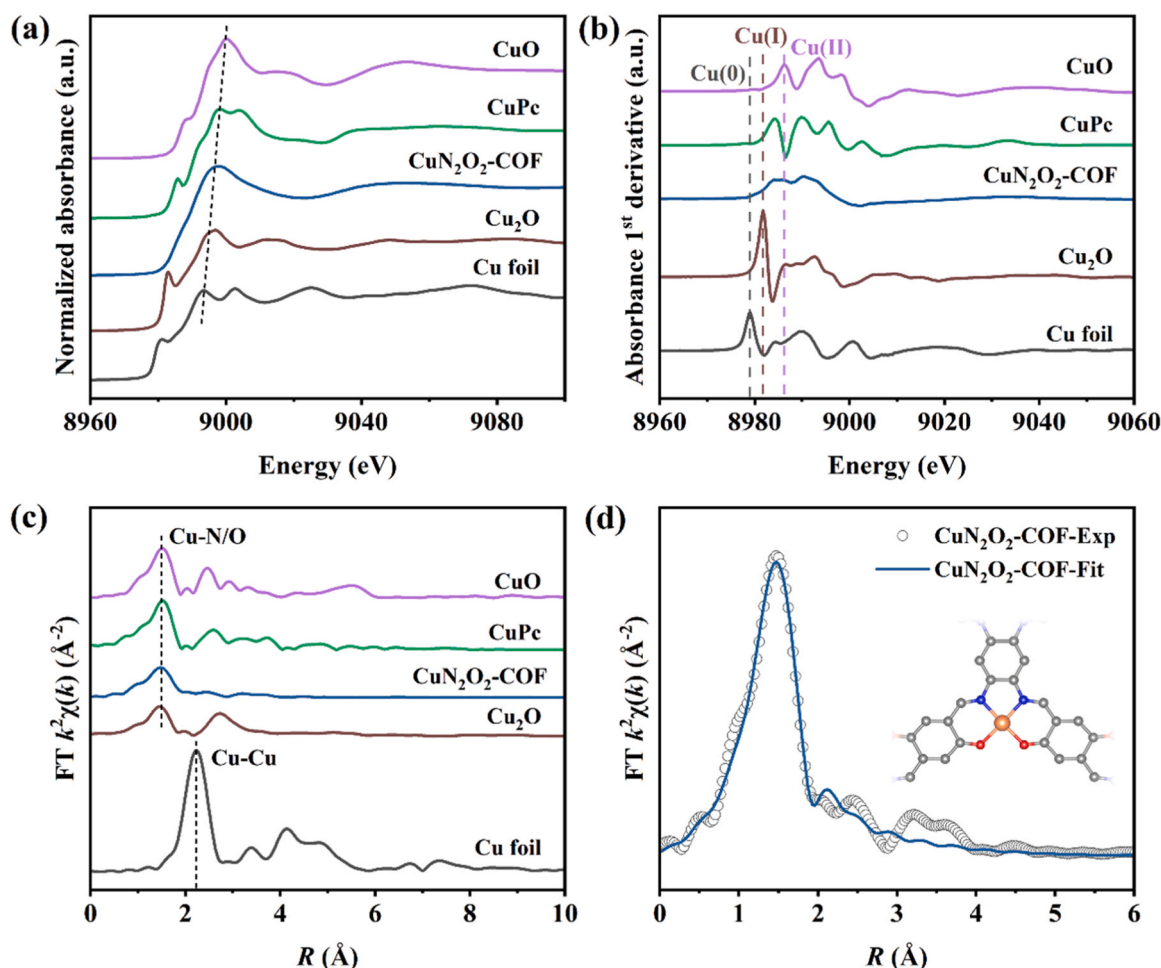


Fig. 4. The Cu K-edge XANES spectra (a), first derivatives of the XANES spectra (b) and Fourier transform Cu K-edge EXAFS spectra (c) for standard Cu foil, Cu_2O , CuPc, CuO and $\text{CuN}_2\text{O}_2\text{-COF}$; EXAFS R-space fitting curves of $\text{CuN}_2\text{O}_2\text{-COF}$ (d). The inset in (d) illustrates the coordination structures of Cu sites in $\text{CuN}_2\text{O}_2\text{-COF}$, where the gray, blue, red, and orange spheres represent C, N, O, and Cu atoms, respectively.

mainly H_2 and a small amount of CO, indicating that $\text{N}_2\text{O}_2\text{-COF}$ had poor selectivity for CO_2ER and high selectivity for the HER. Unlike $\text{N}_2\text{O}_2\text{-COF}$, the $\text{CuN}_2\text{O}_2\text{-COF}$ catalyst generated a large amount of CH_4 in addition to H_2 and CO, and the sum of the FEs of the gaseous products (CH_4 , CO and H_2) was close to 100% at all applied potentials, which was consistent with the fact that no liquid product was detected by ^1H NMR (Fig. S8). The FEs of the different products on $\text{CuN}_2\text{O}_2\text{-COF}$ are shown in Fig. 5c. Compared with $\text{N}_2\text{O}_2\text{-COF}$, $\text{CuN}_2\text{O}_2\text{-COF}$ significantly inhibited the HER and thus had greater selectivity for CO_2ER (Fig. 5b and c). The $\text{FE}(\text{H}_2)$ of $\text{CuN}_2\text{O}_2\text{-COF}$ was less than 50% in the potential range of -1.1 to -1.5 V and reached a minimum of $18.1 \pm 0.8\%$ at -1.3 V. The $\text{FE}(\text{CH}_4)$ of $\text{CuN}_2\text{O}_2\text{-COF}$ gradually increased with the potential from -1.0 to -1.3 V and reached a maximum of $81.2 \pm 1.1\%$ at -1.3 V. Meanwhile, the CH_4 partial current density also gradually increased with the potential from -1.0 V to -1.3 V and reached $20.3 \pm 0.6 \text{ mA}\cdot\text{cm}^{-2}$ at -1.3 V (Fig. S9). However, the $\text{FE}(\text{CH}_4)$ of $\text{CuN}_2\text{O}_2\text{-COF}$ gradually decreased, and the CH_4 partial current density was almost unchanged with a further negative shift in the potential, which may have been caused by limited diffusion of CO_2 in the H-type cell. Moreover, CO was the minor product of $\text{CuN}_2\text{O}_2\text{-COF}$ in the CO_2ER at all potentials, and its FE gradually decreased with increasing negative potential. In particular, the $\text{FE}(\text{CO})$ of $\text{CuN}_2\text{O}_2\text{-COF}$ decreased to less than 1%, and thus, more than 99% of the CO_2ER products were CH_4 when the potential was more negative than -1.3 V, indicating that the $\text{CuN}_2\text{O}_2\text{-COF}$ catalyst had exclusive selectivity for CH_4 in the CO_2ER .

To improve mass transfer during CO_2ER , the $\text{CuN}_2\text{O}_2\text{-COF}$ catalyst

was also tested in a flow cell (Fig. S10) with a standard three-electrode and anion exchange membrane configuration and using a 1 M KOH aqueous solution as the electrolyte. The LSV curves for $\text{CuN}_2\text{O}_2\text{-COF}$ in the flow cell are shown in Fig. 5d. The $\text{CuN}_2\text{O}_2\text{-COF}$ catalyst in the flow cell exhibited a more positive onset potential and larger current density than those in the H-type cell (Fig. 5a and d). In the CO_2 -saturated electrolyte, the current density in the flow cell reached $490 \text{ mA}\cdot\text{cm}^{-2}$ at -1.4 V, which was approximately 21 times greater than that in the H-type cell ($23 \text{ mA}\cdot\text{cm}^{-2}$) at -1.4 V, indicating that the flow cell significantly improved the activity of $\text{CuN}_2\text{O}_2\text{-COF}$ in CO_2ER . The FEs of different products from $\text{CuN}_2\text{O}_2\text{-COF}$ were determined by potentiostatic electrolyses in the flow cell and the results are shown in Fig. 5e. On $\text{CuN}_2\text{O}_2\text{-COF}$, CH_4 was the main product, H_2 , CO and C_2H_4 were minor products, and almost no liquid product was detected (Fig. S11). The $\text{FE}(\text{H}_2)$ of $\text{CuN}_2\text{O}_2\text{-COF}$ was less than 25% in the whole test range and reached a minimum of $8.0 \pm 0.1\%$ at -1.3 V, indicating that the flow cell more effectively inhibited the HER than did the H-type cell. More importantly, compared with that of the H-type cell, the selectivity for CH_4 in the flow cell was also significantly higher: the $\text{FE}(\text{CH}_4)$ of $\text{CuN}_2\text{O}_2\text{-COF}$ was greater than 70% over a wide potential range (-1.1 to -1.5 V) and reached a maximum of $85.4 \pm 1.1\%$ at -1.3 V, far exceeding those of most of the electrocatalysts reported for the CO_2ER (Table S3).

In addition, the Cu single sites in many Cu-based MOF/COF materials easily agglomerate into metallic Cu clusters or nanoparticles during CO_2ER , which leads to the collapse of their intrinsic active sites [48,49].

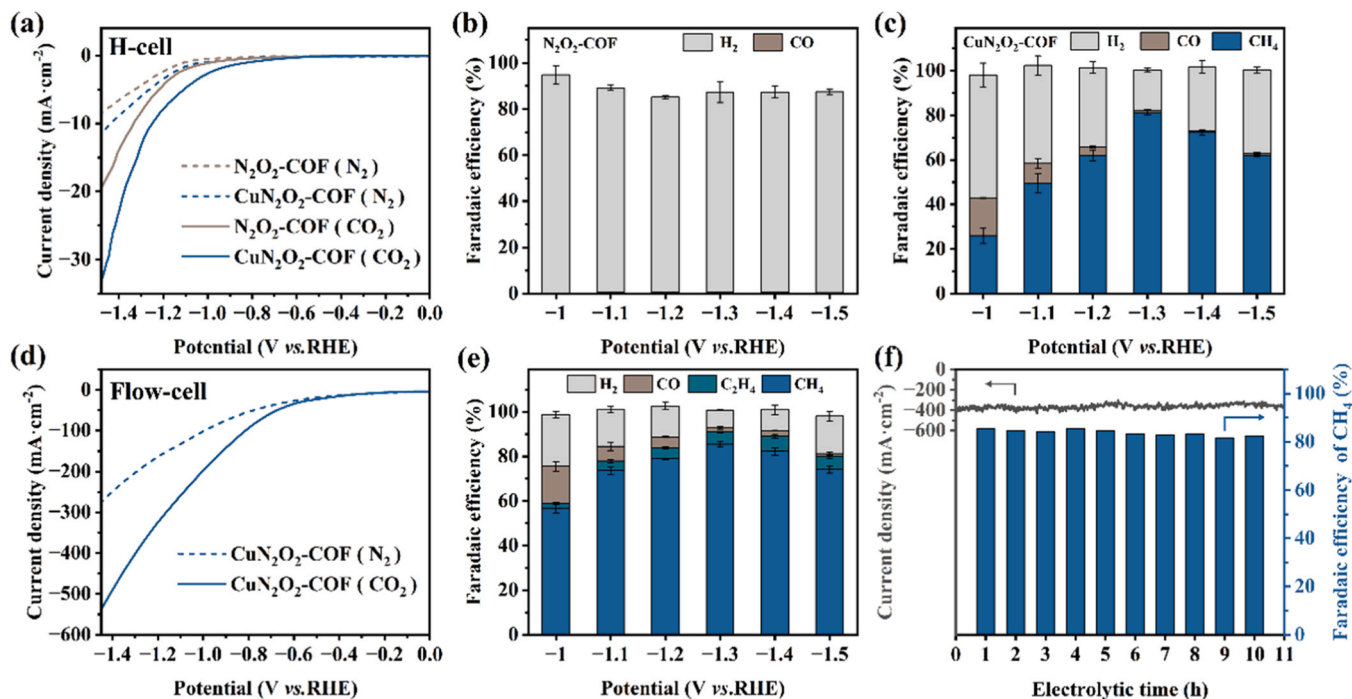


Fig. 5. LSV curves of $\text{N}_2\text{O}_2\text{-COF}$ and $\text{CuN}_2\text{O}_2\text{-COF}$ measured in N_2 - and CO_2 -saturated 0.5 M KHCO_3 (a); the FEs for the products formed on $\text{N}_2\text{O}_2\text{-COF}$ (b) and $\text{CuN}_2\text{O}_2\text{-COF}$ (c) in the H-cell. LSV curves of $\text{CuN}_2\text{O}_2\text{-COF}$ measured in N_2 - and CO_2 -saturated 1 M KOH (d) and the FEs for products formed on $\text{CuN}_2\text{O}_2\text{-COF}$ in the flow cell (e); stability test of $\text{CuN}_2\text{O}_2\text{-COF}$ at -1.3 V (f).

To assess the stability of $\text{CuN}_2\text{O}_2\text{-COF}$ during CO_2ER , prolonged potentiostatic electrolysis was performed at an optimal potential of -1.3 V. As shown in Fig. 5f, the $\text{FE}(\text{CH}_4)$ of $\text{CuN}_2\text{O}_2\text{-COF}$ remained above 80%, and the total current density remained almost constant after electrolysis for 10 h. In addition, the XRD, XPS and TEM results showed that there were no metallic Cu clusters in $\text{CuN}_2\text{O}_2\text{-COF}$ after the prolonged reaction, and the structure and morphology as well as the valence of the Cu single sites in $\text{CuN}_2\text{O}_2\text{-COF}$ were almost the same after the prolonged reaction as those before the reaction (Figs. S12 and S13). The above results demonstrated that the $\text{CuN}_2\text{O}_2\text{-COF}$ catalyst was stable during the CO_2ER .

3.3. Influence of the Cu-coordinated configurations in Cu-based MOFs/COFs on their CO_2ER performance

To explore the relationship between the coordination configurations of the Cu sites in Cu-based MOF/COF materials and their CO_2ER performance, typical CuPc containing Cu-N_4 sites and Cu-THQ containing Cu-O_4 sites were adopted as reference catalysts for CO_2ER studies in this work. The molecular structures of the three catalysts with different coordination configurations are shown in Fig. 6a. The XRD, SEM and XPS results for CuPc and Cu-THQ were consistent with those reported in the literature (Figs. S14 and S15) [50–52], which proved that the two reference catalysts were successfully obtained. The LSV curves of CuPc and Cu-THQ measured in the flow cell are shown in Fig. 6b. Compared with $\text{CuN}_2\text{O}_2\text{-COF}$, CuPc and Cu-THQ had more negative onset potentials and significantly lower current densities in the CO_2 -saturated electrolyte. The total current density of $\text{CuN}_2\text{O}_2\text{-COF}$ ($490\text{ mA}\cdot\text{cm}^{-2}$) at -1.4 V was approximately 2.3 and 1.4 times greater than those of CuPc ($213\text{ mA}\cdot\text{cm}^{-2}$) and Cu-THQ ($345\text{ mA}\cdot\text{cm}^{-2}$), respectively, indicating that $\text{CuN}_2\text{O}_2\text{-COF}$ with $\text{Cu-N}_2\text{O}_2$ single sites had much greater activity in the CO_2ER than CuPc and Cu-THQ.

The FEs of different products formed on CuPc and Cu-THQ were determined by potentiostatic electrolyses and the results are shown in Fig. S16. Both CuPc and Cu-THQ had high HER selectivities, and the FEs (H_2) of CuPc and Cu-THQ were greater than that of $\text{CuN}_2\text{O}_2\text{-COF}$ over

the whole test range (Fig. S16b). In addition, the main product of CO_2ER on CuPc and Cu-THQ was CH_4 , and the $\text{FE}(\text{CH}_4)$ of the two reference catalysts first increased and then decreased with increasingly negative potentials, reaching a maximum at -1.3 V (Figs. S16c and S16d), which was consistent with the trend for the $\text{FE}(\text{CH}_4)$ of $\text{CuN}_2\text{O}_2\text{-COF}$ (Fig. 5e). However, the $\text{FE}(\text{CH}_4)$ of CuPc and Cu-THQ were lower than that of $\text{CuN}_2\text{O}_2\text{-COF}$ over the whole test range (Fig. 6c). The maximum $\text{FE}(\text{CH}_4)$ values for CuPc and Cu-THQ were $37.7 \pm 1.2\%$ and $68.0 \pm 1.1\%$, respectively, which were significantly lower than the maximum of $85.4 \pm 1.1\%$ for $\text{CuN}_2\text{O}_2\text{-COF}$. In Fig. 6d, $\text{CuN}_2\text{O}_2\text{-COF}$ showed the highest CH_4 partial current density over the whole test range, reaching $313 \pm 4\text{ mA}\cdot\text{cm}^{-2}$ at -1.3 V, which was much greater than those of CuPc ($64 \pm 1\text{ mA}\cdot\text{cm}^{-2}$) and Cu-THQ ($192 \pm 8\text{ mA}\cdot\text{cm}^{-2}$) at -1.3 V. Moreover, the Cu mass-based CH_4 partial current density on $\text{CuN}_2\text{O}_2\text{-COF}$ was as high as $12.91 \pm 0.17\text{ A}\cdot\text{g}_{\text{Cu}}^{-1}$ at -1.3 V, which much exceeded those on CuPc ($2.49 \pm 0.02\text{ A}\cdot\text{g}_{\text{Cu}}^{-1}$) and Cu-THQ ($3.11 \pm 0.13\text{ A}\cdot\text{g}_{\text{Cu}}^{-1}$) at -1.3 V (Fig. S17). The turnover frequencies (TOF) for CH_4 formation on the three catalysts were also calculated, and the results are shown in Fig. 6e. The TOF for the CH_4 formed on $\text{CuN}_2\text{O}_2\text{-COF}$ increased with increasingly negative potential and reached $1.06 \pm 0.01\text{ s}^{-1}$ at -1.3 V, which was 5.3 and 4.1 times greater than those of CuPc ($0.20 \pm 0.01\text{ s}^{-1}$) and Cu-THQ ($0.26 \pm 0.01\text{ s}^{-1}$) at -1.3 V, respectively. The above results demonstrated that $\text{CuN}_2\text{O}_2\text{-COF}$ with $\text{Cu-N}_2\text{O}_2$ single sites exhibited much greater activity and CH_4 selectivity in CO_2ER than CuPc with Cu-N_4 sites and Cu-THQ with Cu-O_4 sites.

To elucidate the reason for the higher activity of $\text{CuN}_2\text{O}_2\text{-COF}$ compared to CuPc and Cu-THQ in CO_2ER , the double-layer capacitance (C_{dl}) was first determined by collecting the cyclic voltammetry (CV) curve in the non-Faradaic interval (0.45–0.55 V) to evaluate the electrochemically active surface area (ECSA) of the catalyst. The CV curves of the three catalysts determined at different scanning rates are shown in Fig. S18, and the corresponding C_{dl} values are shown in Fig. 6f. The C_{dl} value of $\text{CuN}_2\text{O}_2\text{-COF}$ ($4.2\text{ mF}\cdot\text{cm}^{-2}$) was close to that of CuPc ($3.0\text{ mF}\cdot\text{cm}^{-2}$) and lower than that of Cu-THQ ($7.3\text{ mF}\cdot\text{cm}^{-2}$), indicating that the superior activity of $\text{CuN}_2\text{O}_2\text{-COF}$ in the CO_2ER originated from the intrinsic activity of its $\text{Cu-N}_2\text{O}_2$ sites rather than a higher ECSA. In

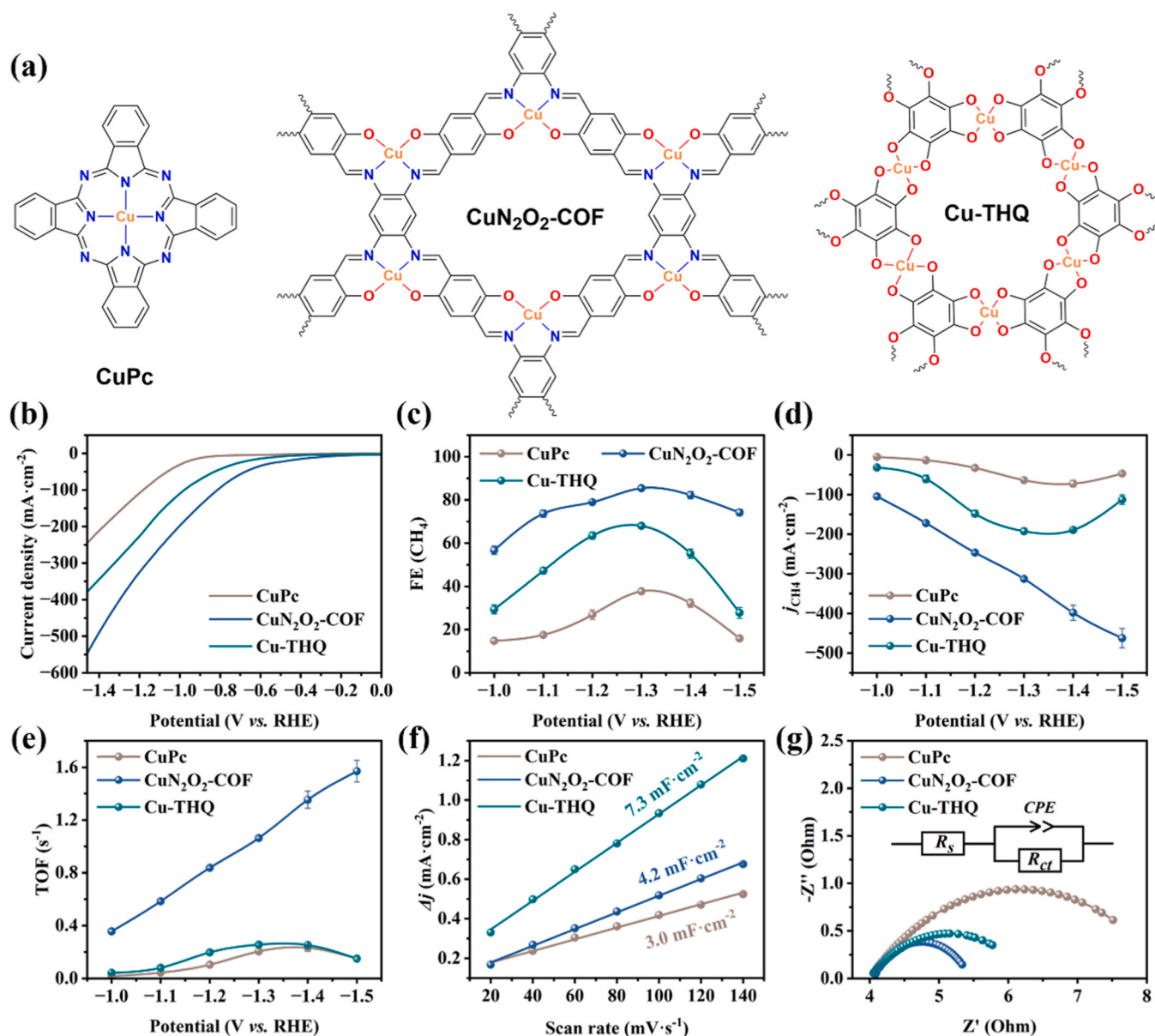


Fig. 6. Molecular structures (a), LSV curves in CO₂-saturated 1 M KOH (b), the FEs of CH₄ (c), CH₄ partial current densities (d), TOFs (e), electrochemically active surface areas (f) and Nyquist plots at -1.3 V (g) for CuPc, CuN₂O₂-COF and Cu-THQ. The inset in (g) represents the fitting equivalent circuit.

addition, the electrochemical impedance spectroscopy (EIS) in Fig. 6g showed that the Nyquist curve for CuN₂O₂-COF had a smaller radius of curvature than those for CuPc and Cu-THQ, indicating that the charge transfer resistance (*R*_{ct}) of CuN₂O₂-COF was the lowest among the three catalysts, which enabled rapid transfer of electrons in the CO₂ER process [53].

It is generally believed that the adsorption of CO₂ on a catalyst is a prerequisite for electroreduction [54], so the CO₂ adsorption isotherms of the three catalysts were measured at 25 °C, and the results are shown in Fig. 7a. Compared with CuPc and Cu-THQ, CuN₂O₂-COF had a greater adsorption capacity for CO₂, and its CO₂ uptake reached a maximum of 5.1 cm³·g⁻¹, which was 17.6 and 1.9 times greater than those of CuPc and Cu-THQ, respectively. The higher CO₂ adsorption capacity of CuN₂O₂-COF facilitated activation and the subsequent reduction of CO₂ [55]. It is commonly accepted that electroreduction of CO₂ adsorbed on a catalyst surface to CH₄ occurs via formation of the *CO intermediate, but the pathway of *CO reduction to CH₄ is still controversial [4,5]. In situ electrochemical ATR-FTIR spectroscopy was used to determine the intermediates and reaction pathway of CO₂ER to CH₄ on CuN₂O₂-COF,

and the results are shown in Fig. 7b. The peaks at 1649, 1410, 1346 and 1268 cm⁻¹ were attributed to the asymmetric stretching, symmetric stretching, C-O stretching and O-H deformation vibrations of *COOH [56,57], respectively, indicating the presence of *COOH intermediates during the reaction. The peak at 2095 cm⁻¹ was assigned to the *CO intermediate [38,58]. In addition, the peaks at 1031, 1458 and 1163 cm⁻¹ corresponded to *CHO, *OCH₂ and *OCH₃ intermediates [48,59], respectively, which were the key intermediates in the pathway of *CO reduction to CH₄ [56,60].

Based on the in situ ATR-FTIR results, the most likely reaction pathway for CO₂ER to CH₄ on CuN₂O₂-COF was proposed, as shown in Fig. 7c. The CO₂ molecule was first adsorbed on the Cu site of CuN₂O₂-COF and underwent a proton-coupled electron transfer (PCET) process to form the *COOH intermediate, which subsequently dehydrated to form the *CO intermediate through another PCET process. Then, the *CO adsorbed on the catalyst was sequentially converted into *CHO, *OCH₂, and *OCH₃ intermediates through a series of PCET processes and finally reduced to CH₄. After CH₄ desorption, the *OH intermediate adsorbed on the catalyst was reduced to H₂O in the subsequent PCET

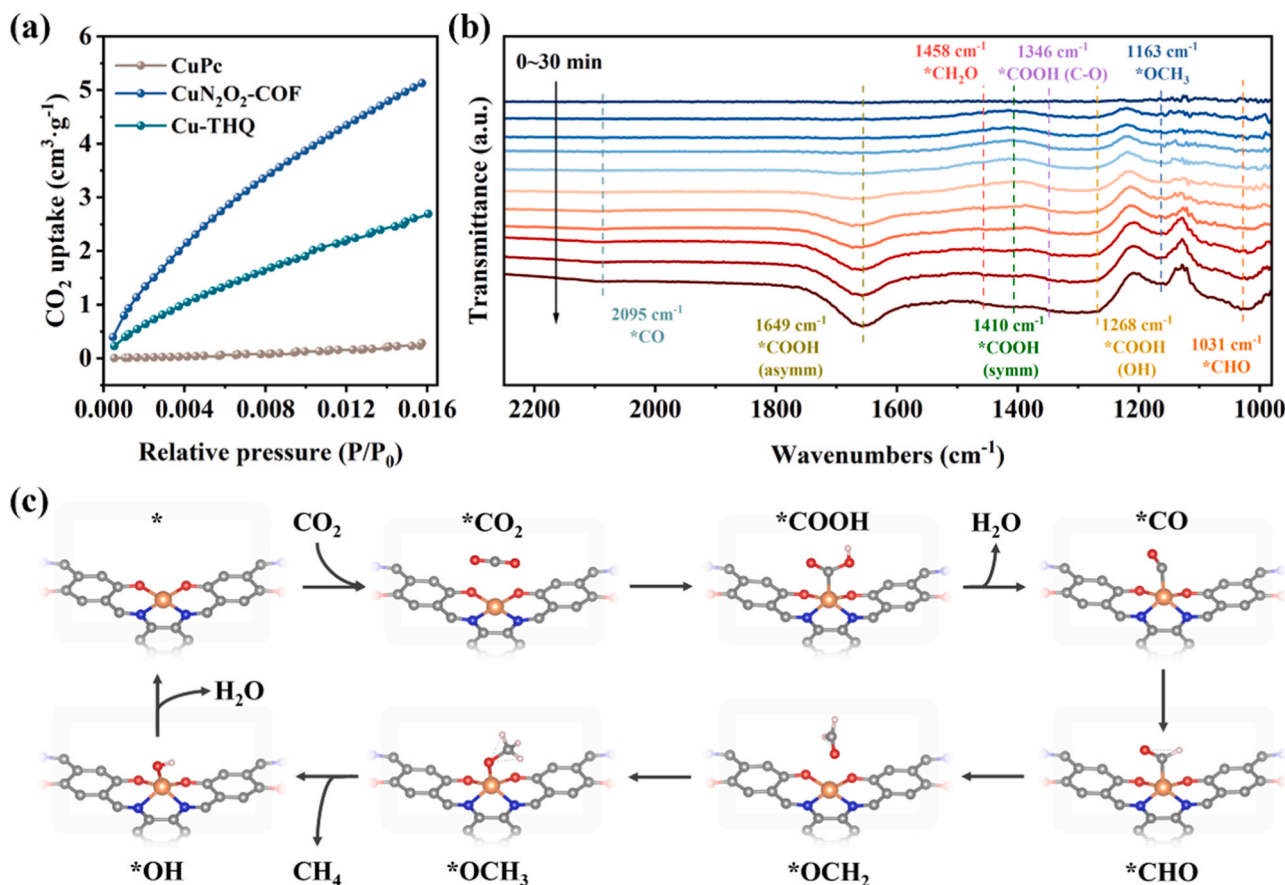


Fig. 7. CO₂ adsorption isotherms of CuPc, CuN₂O₂-COF and Cu-THQ at 25 °C (a). In situ ATR-FTIR spectra of CuN₂O₂-COF collected at -1.3 V in a CO₂-saturated 0.5 M KHCO₃ electrolyte (b). The reaction pathway of CO₂ER to CH₄ on CuN₂O₂-COF (c).

process and finally desorbed to release the active sites of the catalyst for the next reduction reaction.

In addition, density functional theory (DFT) calculations were used to explore the reasons for the different CH₄ selectivities of the three catalysts with different coordination configurations in CO₂ER. The calculated models of CuPc, CuN₂O₂-COF and Cu-THQ are shown in Fig. S19, which were consistent with the molecular structures of the three catalysts (Fig. 6a). First, the effects of the different coordination configurations on the electronic structures of the Cu sites were analyzed by calculating the partial density of states (PDOS) for the Cu 3d orbitals, and the results are shown in Fig. 8a. The d-band center of the Cu 3d orbital in CuN₂O₂-COF was at -2.44 eV, which was more positive than those of CuPc (-3.37 eV) and Cu-THQ (-2.52 eV), indicating that the configuration of the Cu atom coordinated with N and O in CuN₂O₂-COF increased the d-band center of the Cu sites, which facilitated the adsorption of CO₂ and intermediates at the Cu sites [38,61]. Therefore, CuN₂O₂-COF exhibited greater CO₂ uptake than CuPc and Cu-THQ in the above CO₂ adsorption experiment (Fig. 7a).

With the reaction pathway for CO₂ER to CH₄ proposed above (Fig. 7c), the Gibbs free energies of the intermediates on the three catalysts were calculated. The structures of the intermediates involved are shown in Figs. S20–S22, and the calculated results are shown in Fig. 8b–d. The variation trends for the Gibbs free energies of the intermediates on CuN₂O₂-COF (Cu-N₂O₂ site) were similar to those on CuPc (Cu-N₄ site) and Cu-THQ (Cu-O₄ site). In all single-step reactions, *CO₂ → *COOH, *CO → *CHO, and *OCH₂ → *OCH₃ were nonspontaneous (i.e., ΔG > 0). Among these single-step reactions, the step converting the CO₂ molecule into the *COOH intermediate through a PCET process was the potential-determining step (PDS) on the three catalysts because it had the highest energy barrier during CO₂ER. The energy barriers of the

PDSs on the Cu-N₄ site of CuPc and the Cu-O₄ site of Cu-THQ were 2.10 and 1.35 eV, respectively (Fig. 8b and d), while that on the Cu-N₂O₂ site of CuN₂O₂-COF was only 0.90 eV (Fig. 8c). In addition, *CO → *CHO was the key step for CH₄ generation, and its energy barriers on CuPc and Cu-THQ were 1.12 and 0.96 eV, respectively, which were also higher than that of 0.65 eV on CuN₂O₂-COF. The lower energy barrier on CuN₂O₂-COF relative to those on CuPc and Cu-THQ indicated that CuN₂O₂-COF was more reactive in CO₂ER to CH₄ than CuPc and Cu-THQ. As a consequence, CuN₂O₂-COF should exhibit the highest CH₄ selectivity among the three catalysts, which was confirmed by the CO₂ER tests (Fig. 6c–e).

Finally, on CuPc and Cu-THQ, the energy barriers for the formation of the *H intermediate in the HER pathway were 2.03 and 1.29 eV, respectively, which were lower than those of the *COOH intermediate in the CO₂ER pathway (2.10 and 1.35 eV, respectively; Fig. 8b and d). As a consequence, CuPc and Cu-THQ should have high selectivities for the HER, which was demonstrated in the CO₂ER tests (Figs. S16b and S16c). In contrast, the energy barrier for the formation of the *H intermediate (0.98 eV) on CuN₂O₂-COF in Fig. 8c was greater than that for the *COOH intermediate (0.90 eV). Moreover, the adsorption energies of CO₂ and H on the Cu-N₂O₂ site were -0.11 and 0.81 eV, respectively (Fig. S23). The more negative adsorption energy of CO₂ than the one of H indicated that the CO₂ molecule would preferentially occupy the Cu-N₂O₂ sites in the CuN₂O₂-COF catalyst. Therefore, CuN₂O₂-COF could inhibit the HER and promote the CO₂ER, which was also confirmed in the CO₂ER tests (Fig. 5e).

Overall, compared with the Cu-N₄ site of CuPc and the Cu-O₄ site of Cu-THQ, the Cu-N₂O₂ configuration of CuN₂O₂-COF increased the d-band center of the Cu sites and reduced the energy barriers for the formation of key intermediates (i.e., *COOH and *CHO) in the pathway of

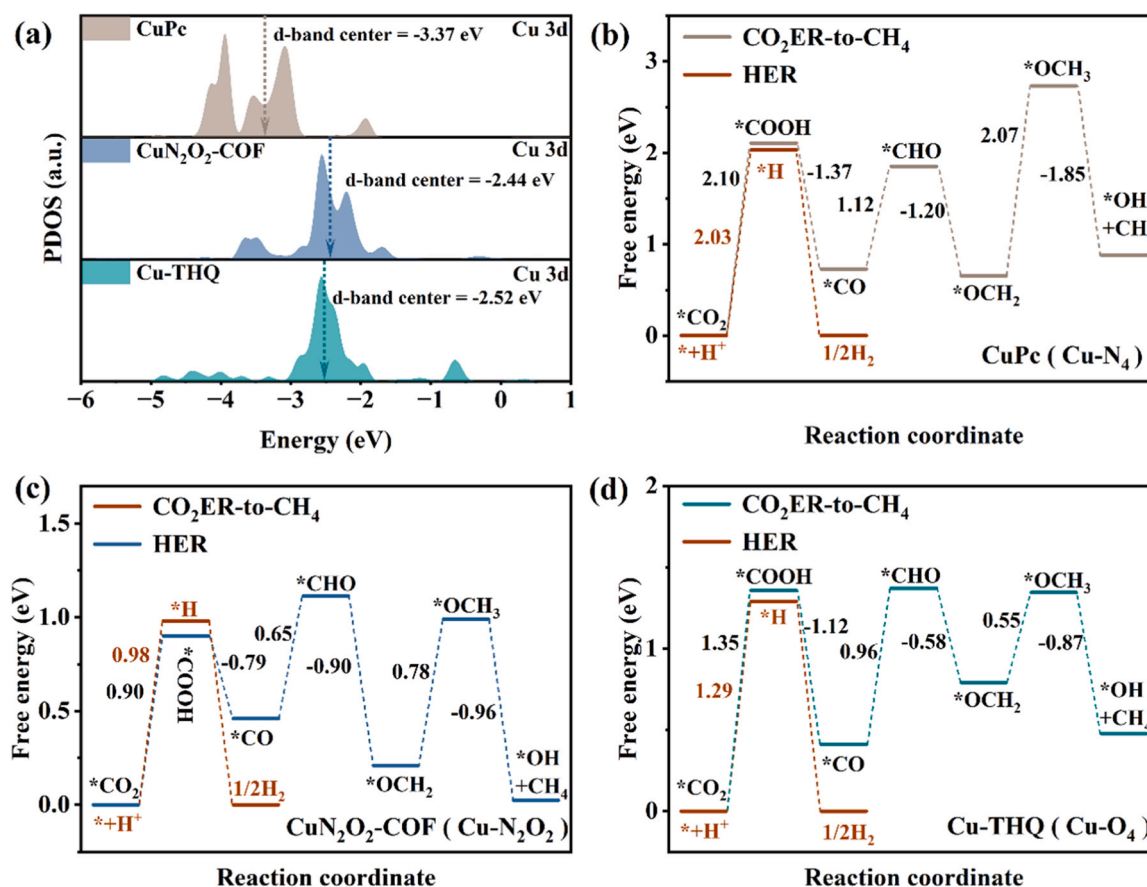


Fig. 8. PDOS of Cu 3d orbitals in CuPc, CuN₂O₂-COF and Cu-THQ (a); free-energy diagrams for CO₂ER to CH₄ and HER on the Cu-N₄ site of CuPc (b), the Cu-N₂O₂ site of CuN₂O₂-COF (c) and the Cu-O₄ site of Cu-THQ (d).

CO₂ER to CH₄, thus accomplishing efficient generation of CH₄.

4. Conclusions

A novel Cu-based COF electrocatalyst for efficient CO₂ER to CH₄ was designed and synthesized in this work. Compared with the typical CuPc containing Cu-N₄ sites and Cu-THQ containing Cu-O₄ sites, the prepared CuN₂O₂-COF catalyst exhibited a higher CH₄ generation efficiency in the CO₂ER due to its abundant Cu-N₂O₂ single sites. The FE(CH₄) of CuN₂O₂-COF reached 81.2% at -1.3 V in the H-type cell, while it further improved to 85.4%, and the CH₄ partial current density reached 313 mA·cm⁻² at -1.3 V, in the flow cell. Moreover, the CuN₂O₂-COF catalyst showed good stability for CH₄ generation during the CO₂ER. The in situ ATR-FTIR results illustrated the reaction pathway of CO₂ER to CH₄ on CuN₂O₂-COF: the adsorbed CO₂ was first reduced to the *COOH intermediate and the subsequent *CO intermediate and then sequentially converted into the *CHO, *OCH₂, and *OCH₃ intermediates and finally reduced to CH₄. The DFT calculations indicated that the higher efficiency for CH₄ generation on CuN₂O₂-COF than on CuPc and Cu-THQ originated from the following phenomena: the Cu-N₂O₂ configuration in CuN₂O₂-COF increased the d-band center of the Cu sites and enhanced the adsorption of key intermediates (i.e., *COOH and *CHO) in the pathway of CO₂ER to CH₄. This work emphasized the importance of Cu-coordinated configurations in Cu-based MOFs/COFs for their CO₂ER performances and provided a new strategy for the design of efficient electrocatalysts for CO₂ER to CH₄.

CRediT authorship contribution statement

Yu Fan: Writing – review & editing, Supervision, Resources, Project

administration, Methodology, Funding acquisition, Conceptualization. **Shuxin Zhong:** Investigation, Formal analysis, Data curation. **Wenli Su:** Writing – original draft, Validation, Investigation, Formal analysis, Data curation.

Declaration of Competing Interest

The authors declare that they have no known competing financial interests or personal relationships that could have appeared to influence the work reported in this paper.

Data Availability

No data was used for the research described in the article.

Acknowledgments

The authors gratefully acknowledge the financial support of Science Foundation of China University of Petroleum, Beijing (Grant No. KYJJ2012-03-03).

Appendix A. Supporting information

Supplementary data associated with this article can be found in the online version at [doi:10.1016/j.apcatb.2024.124145](https://doi.org/10.1016/j.apcatb.2024.124145).

References

- [1] O.S. Bushuyev, P. De Luna, C.T. Dinh, L. Tao, G. Saur, J. van de Lagemaat, S. O. Kelley, E.H. Sargent, What should we make with CO₂ and how can we make it? Joule 2 (2018) 825–832, <https://doi.org/10.1016/j.joule.2017.09.003>.

- [2] P. De Luna, C. Hahn, D. Higgins, S.A. Jaffer, T.F. Jaramillo, E.H. Sargent, What would it take for renewably powered electrosynthesis to displace petrochemical processes? *Science* 364 (2019) eaav3506 <https://doi.org/10.1126/science.aav3506>.
- [3] R. Zhao, P. Ding, P. Wei, L. Zhang, Q. Liu, Y. Luo, T. Li, S. Lu, X. Shi, S. Gao, A. M. Asiri, Z. Wang, X. Sun, Recent progress in electrocatalytic methanation of CO₂ at ambient conditions, *Adv. Funct. Mater.* 31 (2021) 2009449, <https://doi.org/10.1002/adfm.202009449>.
- [4] Y. Lei, Z. Wang, A. Bao, X. Tang, X. Huang, H. Yi, S. Zhao, T. Sun, J. Wang, F. Gao, Recent advances on electrocatalytic CO₂ reduction to resources: Target products, reaction pathways and typical catalysts, *Chem. Eng. J.* 453 (2023) 139663, <https://doi.org/10.1016/j.cej.2022.139663>.
- [5] H. Zheng, Z. Yang, X. Kong, Z. Geng, J. Zeng, Progresses on carbon dioxide electroreduction into methane, *Chin. J. Catal.* 43 (2022) 1634–1641, [https://doi.org/10.1016/S1872-2067\(21\)63967-0](https://doi.org/10.1016/S1872-2067(21)63967-0).
- [6] Z.H. Zhao, J.R. Huang, P.Q. Liao, X.M. Chen, Isolated tin(IV) active sites for highly efficient electroreduction of CO₂ to CH₄ in neutral aqueous solution, *Angew. Chem. Int. Ed.* 62 (2023) e202301767, <https://doi.org/10.1002/anie.202301767>.
- [7] L. Han, S. Song, M. Liu, S. Yao, Z. Liang, H. Cheng, Z. Ren, W. Liu, R. Lin, G. Qi, X. Liu, Q. Wu, J. Luo, H.L. Xin, Stable and efficient single-atom Zn catalyst for CO₂ reduction to CH₄, *J. Am. Chem. Soc.* 142 (2020) 12563–12567, <https://doi.org/10.1021/jacs.9b12111>.
- [8] K. Manthiram, B.J. Beberwyck, A.P. Alivisatos, Enhanced electrochemical methanation of carbon dioxide with a dispersible nanoscale copper catalyst, *J. Am. Chem. Soc.* 136 (2014) 13319–13325, <https://doi.org/10.1021/ja5065284>.
- [9] P. Iyengar, J. Huang, G.L. De Gregorio, C. Gadiyar, R. Buonsanti, Size dependent selectivity of Cu nano-octahedral catalysts for the electrochemical reduction of CO₂ to CH₄, *Chem. Commun.* 55 (2019) 8796–8799, <https://doi.org/10.1039/c9cc02522g>.
- [10] X. Tan, C. Yu, C. Zhao, H. Huang, X. Yao, X. Han, W. Guo, S. Cui, H. Huang, J. Qiu, Restructuring of Cu₂O to Cu₂O@Cu-metal-organic frameworks for selective electrochemical reduction of CO₂, *ACS Appl. Mater. Interfaces* 11 (2019) 9904–9910, <https://doi.org/10.1021/acsami.8b19111>.
- [11] Z. Zhao, X. Peng, X. Liu, X. Sun, J. Shi, L. Han, G. Li, J. Luo, Efficient and stable electroreduction of CO₂ to CH₄ on CuS nanosheet arrays, *J. Mater. Chem. A* 5 (2017) 20239–20243, <https://doi.org/10.1039/c7ta05507b>.
- [12] L. Xue, C. Zhang, J. Wu, Q.-Y. Fan, Y. Liu, Y. Wu, J. Li, H. Zhang, F. Liu, S. Zeng, Unveiling the reaction pathway on Cu/CeO₂ catalyst for electrocatalytic CO₂ reduction to CH₄, *Appl. Catal. B-Environ.* 304 (2022) 120951, <https://doi.org/10.1016/j.apcatb.2021.120951>.
- [13] W. Zhu, L. Zhang, P. Yang, X. Chang, H. Dong, A. Li, C. Hu, Z. Huang, Z.J. Zhao, J. Gong, Morphological and compositional design of Pd–Cu bimetallic nanocatalysts with controllable product selectivity toward CO₂ electroreduction, *Small* 14 (2018) 1703314, <https://doi.org/10.1002/smll.201703314>.
- [14] M.K. Kim, H.J. Kim, H. Lim, Y. Kwon, H.M. Jeong, Metal-organic framework-mediated strategy for enhanced methane production on copper nanoparticles in electrochemical CO₂ reduction, *Electrochim. Acta* 306 (2019) 28–34, <https://doi.org/10.1016/j.electacta.2019.03.101>.
- [15] Y. Zhang, X.Y. Zhang, W.Y. Sun, In situ carbon-encapsulated copper-doped cerium oxide derived from MOFs for boosting CO₂-to-CH₄ electro-conversion, *ACS Catal.* 13 (2023) 1545–1553, <https://doi.org/10.1021/acscatal.2c05538>.
- [16] H. Li, S. Cao, H. Sun, Y. Lu, Y. Zhang, X. Lu, J. Zeng, Z. Yan, CuNCN derived Cu-based/C_N catalysts for highly selective CO₂ electroreduction to hydrocarbons, *Appl. Catal. B-Environ.* 320 (2023) 121948, <https://doi.org/10.1016/j.apcatb.2022.121948>.
- [17] L. Fan, C. Xia, F.Q. Yang, J. Wang, H.T. Wang, Y.Y. Lu, Strategies in catalysts and electrolyzer design for electrochemical CO₂ reduction toward C₂₊ products, *Sci. Adv.* 6 (2020) 17, <https://doi.org/10.1126/sciadv.aay3111>.
- [18] T.K. Todorova, M.W. Schreiber, M. Fontecave, Mechanistic understanding of CO₂ reduction reaction (CO₂RR) toward multicarbon products by heterogeneous copper-based catalysts, *ACS Catal.* 10 (2020) 1754–1768, <https://doi.org/10.1021/acscatal.9b04746>.
- [19] C.E. Creissen, M. Fontecave, Keeping sight of copper in single-atom catalysts for electrochemical carbon dioxide reduction, *Nat. Commun.* 13 (2022) 2280, <https://doi.org/10.1038/s41467-022-30027-x>.
- [20] Q. Wang, C. Cai, M. Dai, J. Fu, X. Zhang, H. Li, H. Zhang, K. Chen, Y. Lin, H. Li, J. Hu, M. Miyauchi, M. Liu, Recent advances in strategies for improving the performance of CO₂ reduction reaction on single atom catalysts, *Small Sci.* 1 (2020) 2000028, <https://doi.org/10.1002/smss.202000028>.
- [21] J. Zhu, L. Lv, S. Zaman, X. Chen, Y. Dai, S. Chen, G. He, D. Wang, L. Mai, Advances and challenges in single-site catalysts towards electrochemical CO₂ methanation, *Energy Environ. Sci.* 16 (2023) 4812–4833, <https://doi.org/10.1039/d3ee02196c>.
- [22] T. Tang, Z. Wang, J. Guan, Optimizing the electrocatalytic selectivity of carbon dioxide reduction reaction by regulating the electronic structure of single-atom M–N–C materials, *Adv. Funct. Mater.* 32 (2022) 2111504, <https://doi.org/10.1002/adfm.202111504>.
- [23] Y. Cai, J. Fu, Y. Zhou, Y.C. Chang, Q. Min, J.J. Zhu, Y. Lin, W. Zhu, Insights on forming N,O-coordinated Cu single-atom catalysts for electrochemical reduction CO₂ to methane, *Nat. Commun.* 12 (2021) 586, <https://doi.org/10.1038/s41467-020-20769-x>.
- [24] Y. Lu, Z. Zhang, H. Wang, Y. Wang, Toward efficient single-atom catalysts for renewable fuels and chemicals production from biomass and CO₂, *Appl. Catal. B-Environ.* 292 (2021) 120162, <https://doi.org/10.1016/j.apcatb.2021.120162>.
- [25] A. Guan, Z. Chen, Y. Quan, C. Peng, Z. Wang, T.-K. Sham, C. Yang, Y. Ji, L. Qian, X. Xu, G. Zheng, Boosting CO₂ electroreduction to CH₄ via tuning neighboring single-copper sites, *ACS Energy Lett.* 5 (2020) 1044–1053, <https://doi.org/10.1021/acsenergylett.0c00018>.
- [26] H. Yang, L. Shang, Q. Zhang, R. Shi, G.I.N. Waterhouse, L. Gu, T. Zhang, A universal ligand mediated method for large scale synthesis of transition metal single atom catalysts, *Nat. Commun.* 10 (2019) 4585, <https://doi.org/10.1038/s41467-019-12510-0>.
- [27] Y. Chen, S. Ji, C. Chen, Q. Peng, D. Wang, Y. Li, Single-atom catalysts: synthetic strategies and electrochemical applications, *Joule* 2 (2018) 1242–1264, <https://doi.org/10.1016/j.joule.2018.06.019>.
- [28] C. Wang, Z. Lv, W. Yang, X. Feng, B. Wang, A rational design of functional porous frameworks for electrocatalytic CO₂ reduction reaction, *Chem. Soc. Rev.* 52 (2023) 1382–1427, <https://doi.org/10.1039/d2cs00843b>.
- [29] J. Wang, H. Hu, S. Lu, J. Hu, H. Zhu, F. Duan, M. Du, Conductive metal and covalent organic frameworks for electrocatalysis: design principles, recent progress and perspective, *Nanoscale* 14 (2022) 277–288, <https://doi.org/10.1039/d1nr06197f>.
- [30] F. Lyu, W. Hua, H. Wu, H. Sun, Z. Deng, Y. Peng, Structural and interfacial engineering of well-defined metal-organic ensembles for electrocatalytic carbon dioxide reduction, *Chin. J. Catal.* 43 (2022) 1417–1432, [https://doi.org/10.1016/S1872-2067\(21\)63980-3](https://doi.org/10.1016/S1872-2067(21)63980-3).
- [31] P. Shao, L.C. Yi, S.M. Chen, T.H. Zhou, J. Zhang, Metal-organic frameworks for electrochemical reduction of carbon dioxide: the role of metal centers, *J. Energy Chem.* 40 (2020) 156–170, <https://doi.org/10.1016/j.jechem.2019.04.013>.
- [32] J. Liu, D. Yang, Y. Zhou, G. Zhang, G. Xing, Y. Liu, Y. Ma, O. Terasaki, S. Yang, L. Chen, Tricycloquinazoline-based 2D conductive metal-organic frameworks as promising electrocatalysts for CO₂ reduction, *Angew. Chem. Int. Ed.* 60 (2021) 14473–14479, <https://doi.org/10.1002/anie.202103398>.
- [33] X. Xiao, L. Zou, H. Pang, Q. Xu, Synthesis of micro/nanoscaled metal-organic frameworks and their direct electrochemical applications, *Chem. Soc. Rev.* 49 (2020) 301–331, <https://doi.org/10.1039/c7cs00614d>.
- [34] D. Narváez-Celada, A.S. Varela, CO₂ electrochemical reduction on metal-organic framework catalysts: current status and future directions, *J. Mater. Chem. A* 10 (2022) 5899–5917, <https://doi.org/10.1039/d1ta10440c>.
- [35] Y.R. Wang, H.M. Ding, X.Y. Ma, M. Liu, Y.L. Yang, Y. Chen, S.L. Li, Y.Q. Lan, Imparting CO₂ electroreduction auxiliary for integrated morphology tuning and performance boosting in a porphyrin-based covalent organic framework, *Angew. Chem. Int. Ed.* 61 (2021) e202114648, <https://doi.org/10.1002/anie.202114648>.
- [36] Y.R. Wang, M. Liu, G.K. Gao, Y.L. Yang, R.X. Yang, H.M. Ding, Y. Chen, S.L. Li, Y. Q. Lan, Implanting numerous hydrogen-bonding networks in a Cu-porphyrin-based nanosheet to boost CH₄ selectivity in neutral-media CO₂ electroreduction, *Angew. Chem. Int. Ed.* 60 (2021) 21952–21958, <https://doi.org/10.1002/anie.202108388>.
- [37] K. Zhang, J. Xu, T. Yan, L. Jia, J. Zhang, C. Shao, L. Zhang, N. Han, Y. Li, Molecular modulation of sequestered copper sites for efficient electroreduction of carbon dioxide to methane, *Adv. Funct. Mater.* 33 (2023) 2214062, <https://doi.org/10.1002/adfm.202214062>.
- [38] Y. Zhang, Q. Zhou, Z.F. Qiu, X.Y. Zhang, J.Q. Chen, Y. Zhao, F. Gong, W.Y. Sun, Tailoring coordination microenvironment of Cu (I) in metal-organic frameworks for enhancing electroreduction of CO₂ to CH₄, *Adv. Funct. Mater.* 32 (2022) 2203677, <https://doi.org/10.1002/adfm.202203677>.
- [39] Y. Zhang, L.-Z. Dong, S. Li, X. Huang, J.-N. Chang, J.-H. Wang, J. Zhou, S.-L. Li, Y.-Q. Lan, Coordination environment dependent selectivity of single-site-Cu enriched crystalline porous catalysts in CO₂ reduction to CH₄, *Nat. Commun.* 12 (2021) 6390, <https://doi.org/10.1038/s41467-021-26724-8>.
- [40] B. Ravel, M. Newville, ATHENA, ARTEMIS, HEPHAESTUS: data analysis for X-ray absorption spectroscopy using IFEFFIT, *J. Synchrotr. Radiat.* 12 (2005) 537–541, <https://doi.org/10.1107/S0909049505012719>.
- [41] T. Li, W.-D. Zhang, Y. Liu, Y. Li, C. Cheng, H. Zhu, X. Yan, Z. Li, Z.-G. Gu, A two-dimensional semiconducting covalent organic framework with nickel(ii) coordination for high capacitive performance, *J. Mater. Chem. A* 7 (2019) 19676–19681, <https://doi.org/10.1039/c9ta07194f>.
- [42] Z. Liang, J. Wang, P. Tang, W. Tang, L. Liu, M. Shakouri, X. Wang, J. Llorca, S. Zhao, M. Heggen, R.E. Dunin-Borkowski, A. Cabot, H.B. Wu, J. Arbiol, Molecular engineering to introduce carbonyl between nickel salophen active sites to enhance electrochemical CO₂ reduction to methanol, *Appl. Catal. B-Environ.* 314 (2022) 121451, <https://doi.org/10.1016/j.apcatb.2022.121451>.
- [43] D. Chakraborty, S. Nandi, D. Mullangi, S. Haldar, C.P. Vinod, R. Vaidyanathan, Cu/Cu₂O nanoparticles supported on a phenol-pyridyl COF as a heterogeneous catalyst for the synthesis of unsymmetrical diynes via glaser-hay coupling, *ACS Appl. Mater. Interfaces* 11 (2019) 15670–15679, <https://doi.org/10.1021/acsami.9b02860>.
- [44] P. Albacete, J.I. Martinez, X. Li, A. Lopez-Moreno, S.A. Mena-Hernando, A. E. Platero-Prats, C. Montoro, K.P. Loh, E.M. Perez, F. Zamora, Layer-stacking-driven fluorescence in a two-dimensional imine-linked covalent organic framework, *J. Am. Chem. Soc.* 140 (2018) 12922–12929, <https://doi.org/10.1021/jacs.8b07450>.
- [45] Y. Liu, S. Li, L. Dai, J. Li, J. Lv, Z. Zhu, A. Yin, P. Li, B. Wang, The synthesis of hexaazatriphenylene-based 2D conjugated copper metal-organic framework for highly selective and stable electroreduction of CO₂ to methane, *Angew. Chem. Int. Ed.* 60 (2021) 16409–16415, <https://doi.org/10.1002/anie.202105966>.
- [46] Y. Misumi, A. Yamaguchi, Z. Zhang, T. Matsushita, N. Wada, M. Tsuchizu, K. Awaga, Quantum spin liquid state in a two-dimensional semiconducting metal-organic framework, *J. Am. Chem. Soc.* 142 (2020) 16513–16517, <https://doi.org/10.1021/jacs.0c05472>.
- [47] G. Han, Y. Zheng, X. Zhang, Z. Wang, Y. Gong, C. Du, M.N. Banis, Y.-M. Yiu, T.-K. Sham, L. Gu, Y. Sun, Y. Wang, J. Wang, Y. Gao, G. Yin, X. Sun, High loading

- single-atom Cu dispersed on graphene for efficient oxygen reduction reaction, *Nano Energy* 66 (2019) 104088, <https://doi.org/10.1016/j.nanoen.2019.104088>.
- [48] J.D. Yi, R. Xie, Z.L. Xie, G.L. Chai, T.F. Liu, R.P. Chen, Y.B. Huang, R. Cao, Highly Selective CO₂ electroreduction to CH₄ by insitu generated Cu₂O single-type sites on a conductive MOF: stabilizing key intermediates with hydrogen bonding, *Angew. Chem. Int. Ed.* 59 (2020) 23641–23648, <https://doi.org/10.1002/anie.202010601>.
- [49] H. Sun, L. Chen, L. Xiong, K. Feng, Y. Chen, X. Zhang, X. Yuan, B. Yang, Z. Deng, Y. Liu, M.H. Rummeli, J. Zhong, Y. Jiao, Y. Peng, Promoting ethylene production over a wide potential window on Cu crystallites induced and stabilized via current shock and charge delocalization, *Nat. Commun.* 12 (2021) 6823, <https://doi.org/10.1038/s41467-021-27169-9>.
- [50] L. Majidi, A. Ahmadiparidari, N. Shan, S.N. Misal, K. Kumar, Z. Huang, S. Rastegar, Z. Hemmat, X. Zou, P. Zapol, J. Cabana, L.A. Curtiss, A. Salehi-Khojin, 2D copper tetrahydroxyquinone conductive metal-organic framework for selective CO₂ electrocatalysis at low overpotentials, *Adv. Mater.* 33 (2021) e2004393, <https://doi.org/10.1002/adma.202004393>.
- [51] Z. Weng, Y. Wu, M. Wang, J. Jiang, K. Yang, S. Huo, X.-F. Wang, Q. Ma, G. W. Brudvig, V.S. Batista, Y. Liang, Z. Feng, H. Wang, Active sites of copper-complex catalytic materials for electrochemical carbon dioxide reduction, *Nat. Commun.* 9 (2018) 415, <https://doi.org/10.1038/s41467-018-02819-7>.
- [52] J. Zhang, T.H. My Pham, Z. Gao, M. Li, Y. Ko, L. Lombardo, W. Zhao, W. Luo, A. Züttel, Electrochemical CO₂ Reduction over Copper Phthalocyanine Derived Catalysts with Enhanced Selectivity for Multicarbon Products, *ACS Catal.* 13 (2023) 9326–9335, <https://doi.org/10.1021/acscatal.3c01439>.
- [53] M. Asadi, K. Kim, C. Liu, A.V. Addepalli, P. Abbasi, P. Yasaei, P. Phillips, A. Behranginia, J.M. Cerrato, R. Haasch, P. Zapol, B. Kumar, R.F. Klie, J. Abiad, L. A. Curtiss, A. Salehi-Khojin, Nanostructured transition metal dichalcogenide electrocatalysts for CO₂ reduction in ionic liquid, *Science* 353 (2016) 467–470, <https://doi.org/10.1126/science.aaf4767>.
- [54] G. Shi, Y. Xie, L. Du, X. Fu, X. Chen, W. Xie, T.B. Lu, M. Yuan, M. Wang, Constructing Cu–C bonds in a graphdiyne-regulated Cu single-atom electrocatalyst for CO₂ reduction to CH₄, *Angew. Chem. Int. Ed.* 61 (2022) e202203569, <https://doi.org/10.1002/ange.202203569>.
- [55] A. Zhang, Y. Liang, H. Li, X. Zhao, Y. Chen, B. Zhang, W. Zhu, J. Zeng, Harmonizing the electronic structures of the adsorbate and catalysts for efficient CO₂ reduction, *Nano Lett.* 19 (2019) 6547–6553, <https://doi.org/10.1021/acs.nanolett.9b02782>.
- [56] X. Li, Y. Sun, J. Xu, Y. Shao, J. Wu, X. Xu, Y. Pan, H. Ju, J. Zhu, Y. Xie, Selective visible-light-driven photocatalytic CO₂ reduction to CH₄ mediated by atomically thin CuInS₂ layers, *Nat. Energy* 4 (2019) 690–699, <https://doi.org/10.1038/s41560-019-0431-1>.
- [57] N.J. Firet, W.A. Smith, Probing the reaction mechanism of CO₂ electroreduction over Ag films via operando infrared spectroscopy, *ACS Catal.* 7 (2017) 606–612, <https://doi.org/10.1021/acscatal.6b02382>.
- [58] S. Zhu, T. Li, W.-B. Cai, M. Shao, CO₂ Electrochemical reduction as probed through infrared spectroscopy, *ACS Energy Lett.* 4 (2019) 682–689, <https://doi.org/10.1021/acsenerylett.8b02525>.
- [59] Y.-Y. Liu, H.-L. Zhu, Z.-H. Zhao, N.-Y. Huang, P.-Q. Liao, X.-M. Chen, Insight into the effect of the d-orbital energy of copper ions in metal–organic frameworks on the selectivity of electroreduction of CO₂ to CH₄, *ACS Catal.* 12 (2022) 2749–2755, <https://doi.org/10.1021/acscatal.1c04805>.
- [60] X. Nie, M.R. Esopi, M.J. Janik, A. Asthagiri, Selectivity of CO₂ reduction on copper electrodes: the role of the kinetics of elementary steps, *Angew. Chem. Int. Ed.* 52 (2013) 2459–2462, <https://doi.org/10.1002/anie.201208320>.
- [61] Z. Chen, X. Zhang, W. Liu, M. Jiao, K. Mou, X. Zhang, L. Liu, Amination strategy to boost the CO₂ electroreduction current density of M–N/C single-atom catalysts to the industrial application level, *Energy Environ. Sci.* 14 (2021) 2349–2356, <https://doi.org/10.1039/d0ee04052e>.